

# Direct $N$ -body simulations of globular clusters – I. Palomar 14

Akram Hasani Zonoozi,<sup>1,2★</sup> Andreas H. W. Küpper,<sup>2,3★</sup> Holger Baumgardt,<sup>2,4★</sup>  
Hosein Haghi,<sup>1,2★</sup> Pavel Kroupa<sup>2★</sup> and Michael Hilker<sup>5★</sup>

<sup>1</sup>*Department of Physics, Institute for Advanced Studies in Basic Sciences (IASBS), PO Box 11365-9161, Zanjan, Iran*

<sup>2</sup>*Argelander Institute für Astronomie (AfA), Auf dem Hügel 71, 53121 Bonn, Germany*

<sup>3</sup>*European Southern Observatory, Alonso de Cordova 3107, Vitacura, Santiago, Chile*

<sup>4</sup>*University of Queensland, School of Mathematics and Physics, Brisbane, QLD 4072, Australia*

<sup>5</sup>*European Southern Observatory, D-85748 Garching b. München, Germany*

Accepted 2010 October 5. Received 2010 October 3; in original form 2010 August 9

## ABSTRACT

We present the first ever direct  $N$ -body computations of an old Milky Way globular cluster over its entire lifetime on a star-by-star basis. Using recent GPU hardware at Bonn University, we have performed a comprehensive set of  $N$ -body calculations to model the distant outer halo globular cluster Palomar 14 (Pal 14). Pal 14 is unusual in that its mean density is about 10 times smaller than that in the solar neighbourhood. Its large radius as well as its low-mass make it possible to simulate Pal 14 on a star-by-star basis. By varying the initial conditions, we aim at finding an initial  $N$ -body model which reproduces the observational data best in terms of its basic parameters, i.e. half-light radius, mass and velocity dispersion. We furthermore focus on reproducing the stellar mass function slope of Pal 14 which was found to be significantly shallower than in most globular clusters. While some of our models can reproduce Pal 14's basic parameters reasonably well, we find that dynamical mass segregation alone cannot explain the mass function slope of Pal 14 when starting from the canonical Kroupa initial mass function (IMF). In order to seek an explanation for this discrepancy, we compute additional initial models with varying degrees of primordial mass segregation as well as with a flattened IMF. The necessary degree of primordial mass segregation turns out to be very high, though, such that we prefer the latter hypothesis which we discuss in detail. This modelling has shown that the initial conditions of Pal 14 after gas expulsion must have been a half-mass radius of about 20 pc, a mass of about  $50\,000\,M_{\odot}$ , and possibly some mass segregation or an already established non-canonical IMF depleted in low-mass stars. Such conditions might be obtained by a violent early gas-expulsion phase from an embedded cluster born with mass segregation. Only at large Galactocentric radii are clusters likely to survive as bound entities the destructive gas-expulsion process we seem to have uncovered for Pal 14. In addition, we compute a model with a 5 per cent primordial binary fraction to test if such a population has an effect on the cluster's evolution. We see no significant effect, though, and moreover find that the binary fraction of Pal 14 stays almost the same and gives the final fraction over its entire lifetime due to the cluster's extremely low density. Low-density, halo globular clusters might therefore be good targets to test primordial binary fractions of globular clusters.

**Key words:** methods: numerical – globular clusters: individual: Palomar 14.

## 1 INTRODUCTION

The initial mass function (IMF) of stars is an important quantity for astrophysics. Since the properties and evolution of a star are closely related to its mass, the IMF is a link between stellar evolution and

the evolution of stellar systems. It influences the chemical evolution of galaxies and the dynamical evolution of star clusters. The IMF is often expressed as a power-law function ( $dN/dm \propto m^{-\alpha}$ ). The traditional IMF that was proposed by Salpeter (1955) from analysing stars in the solar neighbourhood with masses between  $0.4$  and  $10\,M_{\odot}$  has  $\alpha = 2.3$ , implying that high-mass stars are rare compared to low-mass stars. Later advances showed that the IMF slope flattens to  $\alpha = 1.3$  for stars in the mass range  $0.08$ – $0.5\,M_{\odot}$  while it remains Salpeter's for massive stars (Kroupa 2001).

\*E-mail: a.hasani@iasbs.ac.ir (AHZ); akuepper@astro.uni-bonn.de (AHWK); h.baumgardt@uq.edu.au (HB); haggi@iasbs.ac.ir (HH); pavel@astro.uni-bonn.de (PK); mhilker@eso.org (MH)

Since stars in star clusters have similar metallicities, distances and ages, they are the best objects to study the stellar mass function. However, the mass function of stars in clusters evolves through stellar and dynamical evolution and one has to understand how these processes have affected the mass function of stars before one can extract the IMF from the observed mass function (Baumgardt & Makino 2003). For example, as a result of energy equipartition, the heavier stars tend to move towards the cluster centre while lighter stars tend to move further away from the cluster centre. Since observations of stars in globular clusters (GCs) usually are radially limited, the effect of mass segregation has to be considered when deducing the global mass function from the observed local one. Moreover, as a result of preferential loss of low-mass stars, a cluster's mass-to-light ratio evolves differently from that expected from pure stellar evolution, such that dynamical evolution leads to a decrease of the mass-to-light ratio (Baumgardt & Makino 2003; Kruijssen & Mieske 2009; Anders, Lamers & Baumgardt 2009).

While the observed mass function shows local variations, e.g. as a consequence of dynamical mass segregation, the IMF is usually assumed to have no spatial variation throughout a cluster. However star formation simulations indicate that this assumption could be invalid (e.g. Tan, Krumholz & McKee 2006; Krumholz et al. 2009). There is also some observational evidence for deviations from the standard IMF, at low- and high-mass ends, in many star clusters, which might be the result of dynamical evolution (e.g. see Elmegreen 2004, for a review).

Some of the ideas that have been proposed to explain a shallowness of the slope at the high-mass end include primordial mass segregation of stars in the cluster (e.g. Vesperini & Heggie 1997; Kroupa 2002; Mouri & Taniguchi 2002). But so far it is not clear if star clusters were primordially mass segregated from the star formation epoch or obtained mass segregation via dynamical evolution at a later time. Especially for some young star clusters, it has been shown that the observed mass segregation cannot be explained dynamically from an initially unsegregated system (Bonnell & Davies 1998). The early mass loss due to stellar evolution in star clusters leads to shorter lifetimes, and faster expansion, and has a stronger impact on initially segregated clusters than on unsegregated clusters. (Vesperini, McMillan & Portegies Zwart 2009).

Measured mass functions of a sample of GCs surprisingly show that all high concentration clusters have steep mass functions (i.e. larger  $\alpha$ ), while low concentration ones have a smaller  $\alpha$  (De Marchi, Paresce & Pulone 2007). This is puzzling, because concentrated clusters are expected to be dynamically more evolved and thus most of their low-mass stars should have evaporated from the clusters. However, Marks, Kroupa & Baumgardt (2008) showed that for initially mass-segregated clusters, mostly low-mass stars are lost due to gas expulsion which implies a shallower slope in the low-mass range. Indeed this approach allows to deduce the evolution of the very early Milky Way in unprecedented time resolution as it allows us to deduce the changes in the cluster potential induced by gas expulsion and the varying Galactic tidal field (Marks & Kroupa 2010).

Several studies have been done to dynamically model the evolution of star clusters using  $N$ -body simulations. Recently, Harfst, Portegies Zwart & Stolte (2010) modelled the very young Arches cluster to find the best-fitting initial model by comparing simulations with observational data. In this way, they aimed at constraining the parameters for the initial conditions of the cluster such as IMF, size and mass of the cluster by neglecting the Galactic potential and stellar evolution. Moreover, using  $N$ -body simulations, a close correlation between the slope of the low-mass end of the stellar mass

function and the fraction of the initial cluster mass loss has been found by several authors (Vesperini & Heggie 1997; Baumgardt & Makino 2003; Trenti, Vesperini & Pasquato 2010).

In the present paper, we report on simulations of the diffuse outer halo GC Palomar 14 (Pal 14). Pal 14 with a mass of about  $10^4 M_\odot$  and a (3D) half-light radius of 34 pc, is a particularly interesting object to study. It is one of the most extended Galactic GCs and, with a distance of  $\simeq 70$  kpc (Jordi et al. 2009), is also among the outermost clusters of the Milky Way. This large Galactocentric distance and its low stellar mass density make this cluster an ideal candidate to decide between Newtonian gravity and modified Newtonian dynamics (MOND) (Baumgardt, Grebel & Kroupa 2005; Haghi et al. 2009). Its low density suggests that binary stars may be an important issue for interpreting its measured velocity dispersion (Küpper & Kroupa 2010). Its low mass together with its large radius make it also possible to simulate Pal 14 on a star-by-star basis. However, simulations of the evolution of individual GC's long-term evolution have so far been done only with Monte Carlo or Fokker-Planck simulations (Giersz & Heggie 2009). We therefore performed a set of direct  $N$ -body simulations to determine the most likely starting conditions of Pal 14 in terms of total mass, initial half-mass radius and stellar mass function. We also test if primordial mass segregation is necessary to reproduce the observed flattened mass function. Moreover, we check if primordial binaries get frequently disrupted within such a sparse cluster or whether Pal 14 has preserved its primordial binary content. It should be noted that all simulations performed in the present study start once the cluster is gas-free and has settled back into virial equilibrium.

This paper is organized as follows. In Section 2 we describe the observational data we use to compare our simulations to. Our methodology is described in Section 3. In Section 4 we explain the different  $N$ -body set-ups and compare the numerical results with the observed data. Conclusions are given in Section 5.

## 2 OBSERVATIONAL DATA

We use observational data of Hilker (2006) and Jordi et al. (2009) who have presented a spectroscopic and photometric study of Pal 14. Jordi et al. (2009) have obtained the cluster's mass function using *Hubble Space Telescope*/Wide Field Planetary Camera 2 (*HST*/WFPC2) data from the *HST* archive. Moreover, they determined Pal 14's velocity dispersion by measuring the radial velocities of 17 giant stars using the Ultraviolet-Visual Echelle Spectrograph (Dekker et al. 2000) at the Very Large Telescope of the European Southern Observatory in Chile and the High Resolution Echelle Spectrograph (Vogt et al. 1994) on the Keck I telescope.

The distance of Pal 14 from the Sun was derived from the apparent magnitude of the horizontal branch in the colour-magnitude diagram and an isochrone fit to be about  $71 \pm 1.3$  kpc (Jordi et al. 2009). This is closer to the Sun than previous estimates, e.g. Hilker (2006) and Dotter, Sarajedini & Yang (2008) derived larger distances of 74.7 and 79 kpc, respectively. Pal 14 has a projected half-light radius of 1.28 arcmin (Hilker 2006), which was derived from a curve-of-growth analysis of the integrated light of the member stars. This corresponds to a projected half-light radius of  $R_{\text{phl}} = 26.4 \pm 0.5$  pc at the assumed distance of  $71 \pm 1.3$  kpc and implies a 3D half-light radius of about  $35.6 \pm 0.6$  pc.

Jordi et al. derived the age of the cluster to be  $11.5 \pm 0.5$  Gyr by adopting  $[\text{Fe}/\text{H}] = -1.50$  for the metallicity (Harris 1996) from the best isochrone fitting of Dotter et al. (2007). Although previous work has shown that Pal 14 is 3–4 Gyr younger than typical halo GCs with the same metallicity, thus has an age of  $\simeq 10$  Gyr (Sarajedini

1997; Hilker 2006; Dotter et al. 2008), the recent estimated age by Jordi et al. reduces this difference.

The density profile of the cluster does not exhibit a significant ellipticity and the distribution of its stars is compatible with a homogeneous, circular distribution within the uncertainties (Hilker 2006). The core radius and the central surface brightness of the cluster were determined from the best-fitting King (King 1966) profiles. The concentration parameter which is defined as  $c = \log(r_t/r_c)$  is about 0.85 (Hilker 2006), i.e. rather low compared to most Milky Way GCs.

The velocity dispersion of Pal 14 by measuring radial velocities of 17 red giant cluster members has been presented with and without including one probably binary or asymptotic giant branch (AGB) star (hereafter star 15), whose velocity is more than  $3\sigma$  away from the mean of the other stars (Jordi et al. 2009). For the sample including star 15, the global line-of-sight velocity dispersion is  $0.64 \pm 0.15 \text{ km s}^{-1}$ , and without star 15 it is  $0.38 \pm 0.12 \text{ km s}^{-1}$  (Jordi et al. 2009). The quoted uncertainties reflect the  $1\sigma$  error.

The upper boundary of Pal 14's main sequence (MS) corresponds to a magnitude of 23.4 mag at a wavelength of 555 nm. Based on photometric data, Jordi et al. (2009) used the masses given by the 11.5-Gyr isochrone by Dotter et al. (2007), and found that the observed stellar masses on the MS covered the mass range of  $0.495\text{--}0.825 M_\odot$ . The mass function of Pal 14 was found to be flatter than a Kroupa or Salpeter IMF in the observed mass range, and the best-fitting power-law mass function was obtained for a slope of  $\alpha = 1.27 \pm 0.44$ .

The total mass of stars inside the half-light radius and within the mass range  $0.525\text{--}0.825 M_\odot$  has been estimated to be  $M = (2200 \pm 90) M_\odot$ . With the measured slope for masses down to  $0.5 M_\odot$  and using a Kroupa-like mass function,  $\alpha = 1.3$  for masses between  $0.1$  and  $0.5 M_\odot$ , Jordi et al. (2009) estimated the total mass of Pal 14 to be about  $M_{\text{tot}} = 12\,000 M_\odot$  without taking into account stellar remnants. Since this estimated total mass is a derived quantity and not directly measured, we use the number of bright MS stars,  $N_{\text{bs}}$ , to compare with our models, instead. For this aim, we used the star-count data with completeness factor greater than 0.50, which leads to the mass range from  $0.525$  to  $0.795 M_\odot$  and consequently to the number of Pal 14's bright stars  $N_{\text{bs}} = 2954$  [table 3 of Jordi et al. (2009)]. This mass range corresponds to a magnitude range  $27.2 > m_{555} > 23.5$ .  $m_{555}$  is the *HST* filter, *F555W*, that is very similar to Johnson V [fig. 7 of Jordi et al. (2009)]. The stellar mass at the MS turn-off point,  $m_{\text{MSTO},0} = 23.44$ , is about  $0.79 M_\odot$  (Dotter et al. 2007). Consequently, the central and average density of the cluster are  $0.1$  and  $0.01 \text{ stars pc}^{-3}$ , respectively. The two-body relaxation time of Pal 14 is about 50 Gyr, i.e. several times larger than a Hubble time.

The total number of giant stars including the red giant branch (RGB) and horizontal branch (HB) stars is also another observable quantity. The photometry published by Hilker (2006) has not covered entirely the cluster (a segment in the west was missing) and was not corrected for foreground/background contamination. Therefore, the numbers in the tables of Hilker (2006) are not complete. We therefore redo a new selection and incompleteness calculation to count all RGB and HB stars. Fig. 1 shows Pal 14's colour-magnitude diagram (CMD). Note that some of the brighter RGB stars on the bluer side might actually be AGB stars. This cannot be differentiated from this photometry. From this CMD, it also becomes clear that it makes no sense to count subgiant branch (SGB) stars. The photometric error is large at those magnitudes and the counts are highly incomplete. The spatial distribution of the observed stars is shown in Fig. 2. We divided the regions into

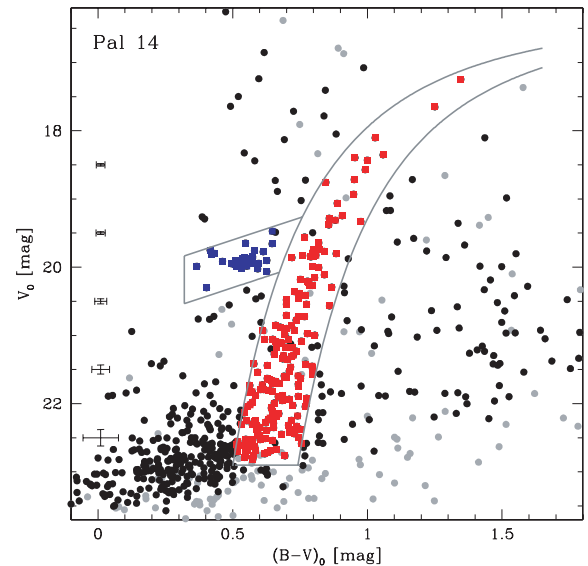


**Figure 1.** Colour-magnitude diagram of Pal 14. The grey dots are all photometric data, the black dots are a selection of point sources with reasonable photometric errors ( $<0.2$  mag). The lines give the selection regions of RGB and HB stars. We put the bottom limit of the RGB to  $V_0 = 22.9$  mag, which would correspond to  $M_{V,0} = 3.48$ . Red squares are those stars in the RGB region that are within the tidal radius of Pal 14. The same applies for the blue squares for the HB stars.

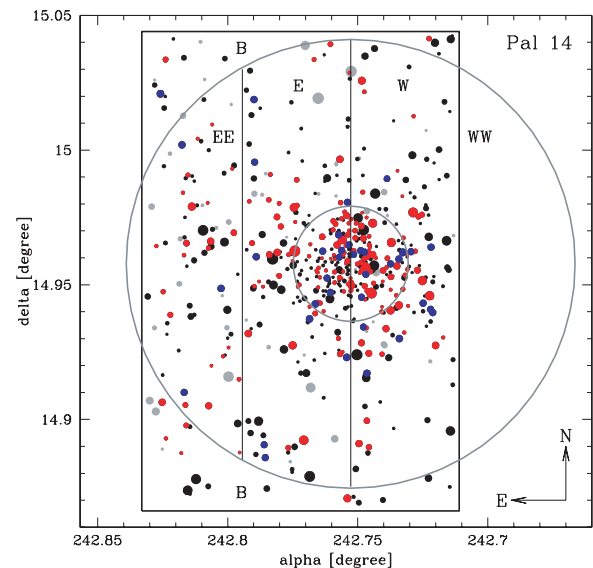


**Figure 2.** Spatial distribution of the photometrically observed Pal 14 stars. The big rectangle marks the area of the observations. The red dots are all objects in the RGB regime shown in the CMD, the blue dots are the objects in the HB area of the CMD. The two large circles are the half-light radius at 1.15 arcmin and the tidal radius of 4.81 arcmin [both from Baumgardt et al. (2005)]. The region is divided into stripes/segments, called EE, E, W and WW from east to west. Everything outside the tidal radius is the background (B) which was used to count the contaminating objects.

stripes/segments, called EE, E, W and WW from east to west. Everything outside the tidal radius is the background (B) which was used to count the contaminating objects. Obviously, the missing region WW should contain more or less the same number of RGB/HB stars as the region EE. But one can also make other sanity checks of number counts, for example whether there are the same amount of

RGB/HB stars in the E and W stripes, or whether really the half-light radius divides the number of RGB/HB stars into half (assuming no mass segregation).

The total area within the tidal radius ( $r < r_t$ ) is 78.5 arcmin<sup>2</sup>. There are different ways to derive the number of RGB and HB stars: (1) assuming that there are as many RGB stars in the WW segment as in the EE segment; (2) doubling the number of RGB stars in the east (E+EE). The first method gives  $N_{\text{RGB}} = 164 \pm 18$ , the second  $N_{\text{RGB}} = 169 \pm 24$ , agreeing very well with the first number. Both values give the background subtracted number counts, taking into account the ratio of the selected area versus the background area, i.e. scaling the background counts to the selected area. This analysis shows that one can safely assume that the RGB counts in the west should be similar to those in the east. Another result is that there are slightly more RGB stars inside the half-light radius,  $N_{\text{RGB}} = 46 \pm 7$ , than outside the half-light radius,  $N_{\text{RGB}} = 39 \pm 10$ . The numbers are consistent within the errors, but might hint to mass segregation of RGB stars on the east side. By the same analysis for the HB stars in the tidal radius we find  $N_{\text{HB}} = 34 \pm 7$  for method (1) and  $N_{\text{HB}} = 33 \pm 10$  for method (2), both values being in very good agreement. The total number of giant stars (RGB+HB),  $N_g = 198 \pm 19$ , is given in the tables to compare with those obtained from the modelled clusters.

In order to reproduce those observational values, e.g. the half-light radius,  $R_{\text{phl}}$ , the number of bright stars,  $N_{\text{bs}}$ , and the mass function slope,  $\alpha$ , we construct a set of  $N$ -body models for Pal 14 in the next section.

### 3 $N$ -BODY MODELS

In total we computed a set of 66 models to find the initial conditions which reproduce the observations of Pal 14 best. The simulations were carried out with the collisional  $N$ -body code NBODY6 (Aarseth 2003) on the GPU computers of the Stellar Population and Dynamics Group of the University of Bonn.

All clusters were set up using the publicly available code *McLUSTER*<sup>1</sup> (Küpper et al., in preparation). We used a Plummer profile in virial equilibrium as initial mass distribution and computed all clusters for 11 Gyr. We chose the initial mass and size (i.e. half-mass radius) of the cluster as free parameters and kept the other parameters of the initial conditions fixed. The number of stars was varied in the range  $7 \times 10^4 < N < 10^5$  such that the clusters have total masses in the range of  $4.6\text{--}5.4 \times 10^4 M_\odot$ . Since the half-mass radius grows due to stellar-evolutionary mass loss and dynamical evolution over the cluster lifetime, we chose the initial 3D half-mass radii in the range of 18–22 pc to reach projected half-light radii of about 26 pc after 11 Gyr.

We have chosen two different IMFs for our models. First, we start with the canonical IMF (Kroupa 2001) using lower and upper mass limits of 0.08 and  $100 M_\odot$ , respectively. At the second step, the clusters were constructed using a flatter mass function with lower and upper mass limits of 0.08 and  $5 M_\odot$ , respectively, mimicking the initial conditions of an initially mass-segregated star cluster after gas expulsion at an age of about 100 Myr. Stellar evolution was modelled according to the routines by Hurley, Pols & Tout (2000). Due to the low escape velocity of Pal 14, we assume a 0 per cent retention fraction for neutron stars and black holes which form during the simulation. Note that the canonical (universal) two-part power-law IMF has  $\alpha_1 = 1.3$  for  $0.08 \leq m \leq 0.5 M_\odot$  and  $\alpha_2 =$

2.3 for  $m \geq 0.5 M_\odot$ . Here we refer to  $\alpha$  as the index of the mass function in the stellar mass range 0.525–0.795  $M_\odot$ .

For simplicity, and since no information on the proper motion is available, the clusters move on a circular orbit through a logarithmic potential,  $\phi(R_G) = V_G^2 \ln R_G$ , of the Milky Way at the assumed distance of Pal 14 and with a circular velocity  $V_G = 220 \text{ km s}^{-1}$ .

All but one cluster do not have primordial binaries. We constructed one model with a primordial binary fraction of 5 per cent to study the impact of binaries on cluster evolution and to estimate the fraction of binaries which dissolve in a Hubble time in a cluster as sparse as Pal 14. The binary population was set up using the Kroupa (1995b) period distribution with random pairing of the binary companions. Random pairing of companion masses for primaries less massive than  $1 M_\odot$  is the correct procedure to reproduce the pre-MS and MS binary-star data (Kroupa 2008).

The modelled clusters were assumed to be not initially mass segregated. In addition, we computed a number of clusters with different degrees of primordial mass segregation to investigate the effect on the cluster's evolution. An overview of the clusters is given in Tables 1, 2 and 3.

### 4 FINDING THE BEST-FITTING MODEL

In order to find the most likely initial conditions, a grid of models with different initial half-mass radii and initial masses was calculated. The main observational values, which were used to compare with each model, are the present-day number of bright MS stars,  $N_{\text{bs}}$ , the present-day projected half-light radius,  $R_{\text{phl}}$ , and the slope of the mass function in the mass range 0.525–0.795  $M_\odot$  within the half-light radius,  $\alpha$ , with values

$$N_{\text{bs}} = 2954 \pm 175, \quad (1)$$

$$R_{\text{phl}} = (26.4 \pm 0.5) \text{ pc} \quad (2)$$

$$\alpha = 1.27 \pm 0.44. \quad (3)$$

Note that, to match  $R_{\text{phl}}$  in the  $N$ -body models, we use only the giant stars since the projected half-light radius comes from Hilker (2006) and he could only see the giant stars in Pal 14. Moreover, for  $N_{\text{bs}}$  we count the MS stars inside the half-light radius with masses between 0.525 and 0.795  $M_\odot$ . Finally, we extract the mass function for those MS stars within the half-light radius, with a mass in the range of  $0.525 M_\odot < m < 0.795 M_\odot$ , i.e. in the same way as Jordi et al. have done. We apply 10 bins between  $\log_{10} m = -0.1$  and  $\log_{10} m = -0.3$ . We reject the lowermost point in the observational data of Jordi et al., since it has a relatively high incompleteness correction, i.e. uncertainty. Since compact remnants are unobservable in Pal 14, as they are too faint, we ignored them in our measurement of the mass function.

To compare our models in an objective way and to measure the quality of the fit of the model to the observations, we define a goodness-of-fit parameter,  $g_p$ . This parameter depends on the model parameters, and measures the closeness between the observations and the model as follow:

$$g_p = 1 - \left| \frac{p_{\text{observation}} - p_{\text{model}}}{p_{\text{observation}}} \right|, \quad (4)$$

where  $p$  represents the corresponding model parameter. The goodness-of-fit parameter ranges from 0 to 1, where 1 describes an excellent fit. Since we have three main observables,  $R_{\text{phl}}$ ,  $N_{\text{bs}}$  and

<sup>1</sup> [www.astro.uni-bonn.de/~akuepper/mcluser/mcluser.html](http://www.astro.uni-bonn.de/~akuepper/mcluser/mcluser.html)

**Table 1.** Details of all  $N$ -body models with regular initial conditions (Section 4.1). The first column gives the model name, in which the first two digit numbers denote the initial mass in  $1000 M_{\odot}$  and the second two digit numbers denote the initial half-mass radius in pc. Columns 2 and 3 are the projected half-mass and half-light radius,  $R_{\text{phm}}$  and  $R_{\text{phl}}$ , respectively. Column 4 is the present-day number of bright MS stars inside the half-light radius, with masses between  $0.525$  and  $0.795 M_{\odot}$ ,  $N_{\text{bs}}$ , whereas column 5 gives the corresponding total mass of these stars.  $\alpha$  is the present-day slope of the mass function for stars with masses between  $0.525$  and  $0.795 M_{\odot}$ . Column 7 is the line-of-sight velocity dispersion. The last column gives the total number of giant stars in the cluster including RGB and HB stars. Typical errors of the numerical values were obtained by repeating runs for a particular model and are indicated in the header. In the last line, the observational values are given for comparison. The subscript ‘\*’ indicates the observed velocity dispersion with taking star 15 into account. Note that none of these models is an acceptable fit to Pal 14.

Model	$R_{\text{phm}}(\text{pc})$ ( $\pm 0.8$ )	$R_{\text{phl}}(\text{pc})$ ( $\pm 2.3$ )	$N_{\text{bs}}$ ( $\pm 260$ )	$M_{r < R_{\text{phm}}}^f (M_{\odot})$ ( $\pm 320$ )	$\alpha$ ( $\pm 0.15$ )	$\sigma_{\text{los}}(\text{km s}^{-1})$ ( $\pm 0.01$ )	$N_{\text{g}}$ ( $\pm 16$ )
M40R15	19.6	15.6	2374	1521	2.10	0.65	162
M40R25	31.5	30.3	2182	1402	1.85	0.51	136
M46R18	23.5	22.0	2912	1869	1.96	0.64	163
M46R19	24.3	19.8	2382	1530	1.90	0.64	161
M46R20	25.8	23.8	2661	1705	2.04	0.61	174
M46R21	28.4	25.2	2407	1542	2.08	0.58	188
M46R22	29.3	26.8	2544	1627	2.10	0.58	160
M48R18	23.7	23.1	3311	2127	1.88	0.66	174
M48R19	24.3	21.5	2847	1821	1.77	0.64	160
M48R20	26.2	22.5	2641	1689	2.13	0.61	172
M48R21	28.0	25.6	2687	1722	2.02	0.59	174
M48R22	28.1	27.6	3079	1970	2.14	0.61	171
M50R18	24.2	21.3	2992	1925	1.78	0.68	194
M50R19	24.5	19.5	2638	1695	1.87	0.65	193
M50R20	26.6	25.8	3108	1995	1.97	0.64	170
M50R21	26.9	24.1	2796	1788	2.14	0.61	178
M50R22	29.3	29.0	2997	1918	2.10	0.60	163
M52R18	24.3	21.5	3181	2038	2.06	0.68	181
M52R19	25.7	24.0	3245	2079	2.00	0.66	186
M52R20	26.6	24.0	2975	1910	1.90	0.65	166
M52R21	28.8	27.0	3027	1939	2.05	0.62	172
M52R22	28.0	29.0	3357	2155	1.98	0.61	171
M54R18	24.0	21.8	3369	2158	2.07	0.70	224
M54R19	25.5	24.8	3556	2279	2.00	0.66	195
M54R20	26.3	25.1	3348	2144	2.08	0.65	161
M54R21	27.9	25.1	3017	1935	1.96	0.63	190
M54R22	30.0	26.0	2865	1834	2.15	0.62	198
M60R25	32.1	33.0	3699	2367	2.22	0.62	170
Observations		$26.4 \pm 0.5$	$2954 \pm 175$	$2200 \pm 90$	$1.27 \pm 0.44$	$0.38 \pm 0.12$ ( $0.64 \pm 0.15^*$ )	$198 \pm 19$

$\alpha$ , we also have three goodness-of-fit parameters,  $g_R$ ,  $g_N$  and  $g_{\alpha}$ , respectively.

There is a significant statistical dispersion in the results if we repeat the calculations for one arbitrary model with the same initial parameters but with a different random seed. The required computational GPU time doesn’t allow us to do statistics for all parameters, though. Hence, in order to estimate the errors of the resulting parameters, we do several runs (10 times) for a particular model and discuss the resulting uncertainty. In the following investigation we will use these uncertainties for our discussion.

In the following sections we will investigate four sets of models. First, we investigate the initial conditions which we call ‘regular’. We assume a Kroupa IMF without primordial mass segregation or primordial binaries. In the second step, we assume that the IMF was flattened within the first 100 Myr through stellar evolution and gas expulsion processes. The third set of models is computed to test how much primordial mass segregation we have to add in order to explain the observed mass function of Pal 14. In the last section, we test the influence of primordial

binaries on the cluster evolution and on the evolution of the mass function.

#### 4.1 Regular initial conditions

Fig. 3 shows how the goodness-of-fit parameters of  $N_{\text{bs}}$ ,  $R_{\text{phl}}$  and  $\alpha$  vary for the different values of the model parameters, initial half-light radius and initial cluster mass. Moreover, the product of the goodness-of-fit parameters for  $N_{\text{bs}}$  and  $R_{\text{phl}}$  is shown in the lower right panel.

The darker areas show where the goodness-of-fit parameters are close to 1 in the parameter space, i.e. show the range in initial conditions that best-fitted to Pal 14. We find that many models (e.g. M54R22, M52R21 and M50R20) can reproduce Pal 14’s half-light radius and its number of bright MS stars.

We look for models whose velocity dispersion lies within the uncertainties of the observational values. Therefore, we take only stars within a clusters tidal radius and with a mass higher than  $0.8 M_{\odot}$ , and measure their velocity dispersion and compare it to

**Table 2.** Details of all  $N$ -body models for three sets of flattened mass functions, with initial slopes of 0.5, 0.6, and 0.7 for stars less massive than  $0.5 M_{\odot}$  (see Section 4.2 for more details). Columns are the same as in Table 1 but in column 2, the first number in the model name is the adopted high-mass slope. Errors are the standard deviations derived from multiple runs with the same parameters (see text). The best-fitting models that agree within the uncertainties with all observational parameters are highlighted with boldface.

	Model	$R_{\text{phm}}$ (pc) ( $\pm 1.6$ )	$R_{\text{phl}}$ (pc) ( $\pm 2.3$ )	$N_{\text{bs}}$ ( $\pm 290$ )	$M_{r < R_{\text{hm}}}^f (M_{\odot})$ ( $\pm 270$ )	$\alpha$ ( $\pm 0.13$ )	$\sigma_{\text{los}} (\text{km s}^{-1})$ ( $\pm 0.03$ )	$N_{\text{g}}$ ( $\pm 25$ )
1	F0.5M45R18	26.7	24.9	2391	1543	1.19	0.59	216
2	F0.5M45R20	28.7	27.5	2322	1476	1.32	0.56	200
3	F0.5M45R22	30.8	29.5	2332	1551	1.53	0.53	216
4	<b>F0.5M50R18</b>	26.9	27.7	3045	1959	1.28	0.62	253
5	<b>F0.5M50R20</b>	29.1	27.7	2635	1678	1.31	0.60	234
6	F0.5M50R22	30.9	30.6	2722	1718	1.16	0.57	242
7	<b>F0.5M55R18</b>	26.0	26.3	3327	2120	1.38	0.66	285
8	<b>F0.5M55R20</b>	29.4	27.2	2824	1819	1.22	0.62	259
9	F0.5M55R22	30.5	29.3	2926	1917	1.38	0.60	268
10	<b>F0.6M45R18</b>	25.2	25.0	2878	1903	1.25	0.61	218
11	F0.6M45R20	27.9	25.5	2493	2017	1.36	0.59	228
12	F0.6M45R22	30.0	28.5	2506	1646	1.60	0.56	210
13	<b>F0.6M50R18</b>	25.9	23.9	2987	1999	1.35	0.64	249
14	<b>F0.6M50R20</b>	27.7	28.0	3133	2001	1.47	0.61	261
15	F0.6M50R22	31.1	31.5	3132	2162	1.51	0.60	217
16	F0.6M55R18	25.4	23.5	3248	2189	1.26	0.68	264
17	<b>F0.6M55R20</b>	27.7	26.1	3358	2155	1.38	0.64	296
18	F0.6M55R22	30.5	29.6	3257	2002	1.36	0.63	275
19	F0.7M45R18	24.3	21.0	2734	1759	1.43	0.68	238
20	<b>F0.7M45R20</b>	26.6	25.6	2971	1926	1.47	0.61	232
21	F0.7M45R22	29.2	29.6	3021	1937	1.74	0.59	222
22	F0.7M50R18	24.4	22.1	3204	2101	1.25	0.68	279
23	<b>F0.7M50R20</b>	26.5	25.1	3324	2172	1.77	0.65	283
24	F0.7M50R22	28.8	28.0	3419	2202	1.47	0.69	272
25	F0.7M55R18	24.4	21.5	3516	2209	1.40	0.72	330
26	F0.7M55R20	26.6	25.5	3773	2526	1.41	0.68	307
27	F0.7M55R22	29.6	27.5	3451	2290	1.45	0.66	289
	Observations		$26.4 \pm 0.5$	$2954 \pm 175$	$2200 \pm 90$	$1.27 \pm 0.44$	$0.38 \pm 0.12$ ( $0.64 \pm 0.15^*$ )	$198 \pm 19$

**Table 3.** Details of all  $N$ -body models with primordial mass segregation and of the one model without primordial mass segregation but with primordial binaries. The mass segregation parameter changes in the range  $S = 0.5$ – $0.95$ ; the binary fraction for the binary model is 0.05. Columns are the same as in Table 1, just in column 1 the first number within the name of the model is here the adopted mass segregation parameter,  $S$ , or the fraction of stars in binaries, respectively. The best-fitting models that agree within the uncertainties with all observational parameters are highlighted with boldface.

Model	$R_{\text{phm}}$ (pc) $\pm 1.2$	$R_{\text{phl}}$ (pc) $\pm 1.9$	$N_{\text{bs}}$ $\pm 120$	$M_{r < R_{\text{hm}}}^f (M_{\odot})$ $\pm 80$	$\alpha$ $\pm 0.10$	$\sigma_{\text{los}} (\text{km s}^{-1})$ $\pm 0.05$	$N_{\text{g}}$ $\pm 8$
S0.50M50R20	29.4	25.3	3184	2044	1.90	0.62	193
S0.60M50R20	32.2	27.5	3209	2061	1.9	0.58	207
S0.70M50R20	32.9	27.9	3267	2106	2.0	0.60	191
S0.80M50R20	35.6	29.6	3219	2066	1.95	0.57	222
S0.90M50R20	42.4	36.0	3257	2100	1.6	0.51	211
S0.91M50R20	43.8	38.5	3365	2169	1.63	0.46	206
S0.93M50R20	47.8	40.6	2887	1870	1.27	0.44	217
S0.95M50R20	48.7	41.5	3159	2045	1.28	0.47	215
<b>S0.95M50R15</b>	37.0	27.6	3077	1978	1.33	0.58	194
<b>S0.90M50R15</b>	33.9	26.3	3236	2085	1.67	0.55	210
B0.04M50R20	27.4	25.3	3132	2009	2.0	0.87	185
Observations		$26.4 \pm 0.5$	$2954 \pm 175$	$2200 \pm 90$	$1.27 \pm 0.44$	$0.38 \pm 0.12$ ( $0.64 \pm 0.15^*$ )	$198 \pm 19$

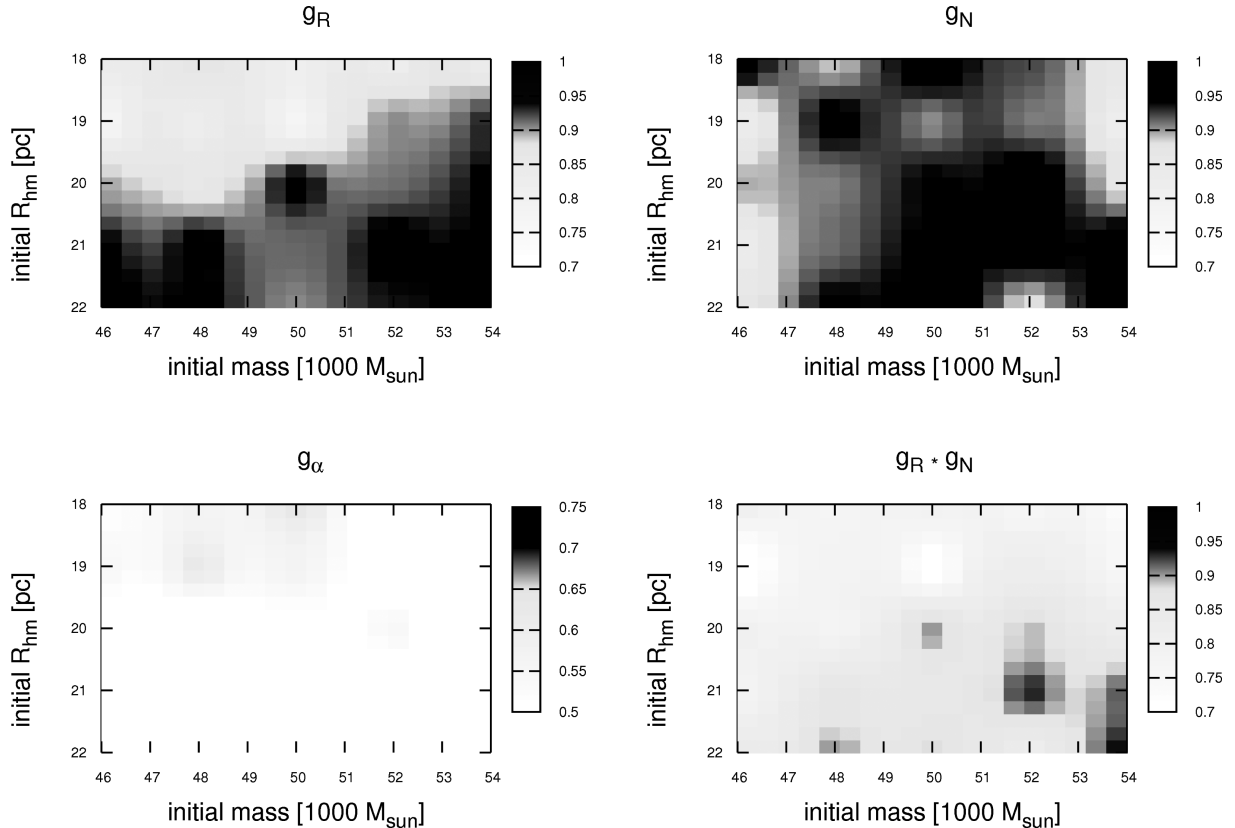


**Figure 3.** Goodness-of-fit parameters from the measured half-light radius (upper left panel), number of bright stars (upper right panel) and mass function slope (lower left panel) for the models with regular initial conditions. In the lower right panel, the product of the two upper panels is given. The varying model parameters are the initial half-mass radius and the cluster initial mass. A goodness-of-fit parameter close or equal to 1 is best and indicated by dark shaded areas in the plots.

the observed value of Jordi et al. (2009). According to Table 1, the line-of-sight velocity dispersion in most of our models is about  $0.6 \text{ km s}^{-1}$ .

Given the small sample size (i.e. radial velocity of 17 stars are used to determine the observed velocity dispersion), the observed velocity dispersion has a large error which could be much larger than the formal error (Gentile et al. 2010). In order to see how well a velocity dispersion of  $\simeq 0.6 \text{ km s}^{-1}$  agrees with the observed one, we use the Kolmogorov–Smirnov (KS) test, which is the applicable statistical test for such a small sample size.

In Fig. 4, we show the cumulative distribution function (cdf) versus radial velocity for both samples with and without star 15, separately. This cdf we compare to the cdf of one of the best-fitting models (M50R20). With star 15, the maximum difference between the two cdfs is 0.13, which corresponds to P-value of 0.94, while in case without star 15 the maximum difference between the two cdfs and corresponding P-values are 0.14 and 0.91, respectively. This means that the models can be rejected with 6 per cent (including star 15) and 9 per cent (excluding star 15) confidence.

In addition, we find that the mean value of the velocity dispersion of all stars is similar to that of the red giant stars and MS stars with masses larger than  $0.8 M_{\odot}$ . Therefore, the velocities of the giants are representative of all stars in the cluster. The number of giant stars,  $N_g$ , is also in most of the modelled clusters in good agreement with the observations.

Fig. 5 shows the mass function of one example model before and after the computation. The red and green points denote the number of stars inside and outside the half-light radius, respectively. We

see that after 11 Gyr, the mass function inside the half-light radius is significantly different from the one outside the half-light radius, which implies that mass segregation has taken place. The mass function of the stars inside the half-light radius is clearly flatter than those of the stars outside. It seems that even in a cluster as large as Pal 14, dynamical mass segregation plays an important role.

According to Table 1 and lower left panel of Fig. 3, the slope of the mass function,  $\alpha$ , in all models is far from the observed value of Pal 14, though, even when accounting for observational errors. The upper limit of the observed value within the  $1\sigma$  error is  $\alpha = 1.71$ , and only if we account for the statistical error for the modelled slope, which is  $\simeq 0.15$ , then two models (i.e. M48R19 and M50R18) are marginally compatible with the observed slope.

Our simulations have typically  $\alpha \simeq 2.0$  after 11 Gyr, i.e. only a mild decrease of the low-mass-star slope from the initial Salpeter value of  $\alpha = 2.35$  due to mass segregation. In contrast, the observed slope is  $\alpha = 1.27 \pm 0.44$ , which agrees with this value only at the  $1.75\sigma$  level. There is therefore some evidence that Pal 14 started with a mass segregated Kroupa IMF.

In order to see whether an extension of the initial parameter space would resolve the problem, we repeat the simulation for some extremely high and low initial values, i.e. we chose 25 and 15 pc for the half-light radius and 40 000 and 60 000  $M_{\odot}$  for the initial mass. The results are shown in Table 1. As can be seen, even by selecting such values for the initial conditions, the present-day mass function of Pal 14 cannot be reproduced. Moreover, we find that the values for  $N_{bs}$  and  $R_{phl}$  get much worse in these directions of the parameter space, showing that we were searching in the right place initially.



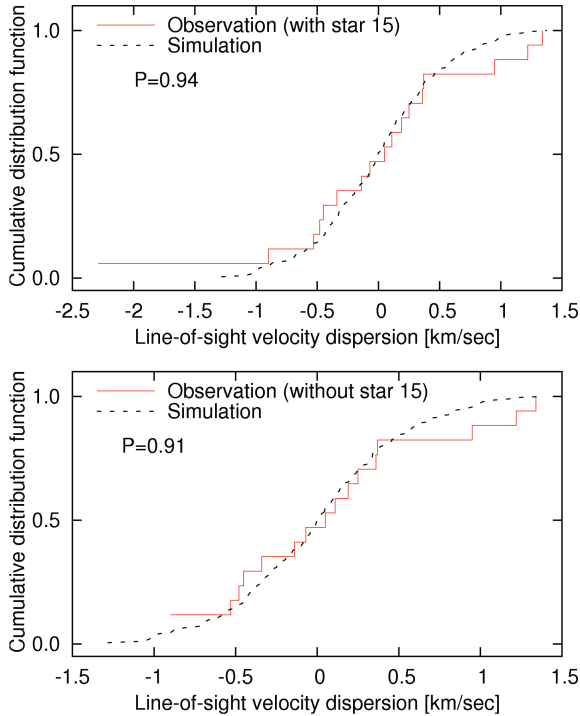


**Figure 4.** The cumulative distribution function (cdf) versus line-of-sight velocity for the sample with star 15 (upper panel) and without star 15 (bottom panel). The solid lines represent the observed data, whereas the dotted line is the cdf of one of the modelled clusters (M50R20). The maximum difference between the two cdfs is 0.13 for the upper panel and 0.14 for the bottom panel, which corresponds to  $P$ -values of 0.94 and 0.91, respectively.

#### 4.2 Flattened mass function

As shown in Section 4.1, the initially unsegregated clusters with a canonical Kroupa IMF cannot reproduce the observed slope of the mass function well. The observed slope is  $\alpha = 1.27 \pm 0.44$  but the slope that could be achieved from  $N$ -body calculations is about 2. In this section, we show that if we choose a flatter IMF for our model, it is possible to explain the observed slope of the mass function.

The evolution and disruption of star clusters due to gas expulsion and stellar evolution may play an important role in the evolution of the GC mass function (GCMF). It has been shown that these early evolutionary processes, i.e. early cluster dissolution due to gas expulsion and mass loss from stellar evolution, can preferentially destroy low-mass clusters and significantly flatten the low-mass end of the power-law initial GCMF (Goodwin 1997; Goodwin 1998; Kroupa & Boily 2002; Baumgardt, Kroupa & Parmentier 2008b; Parmentier et al. 2008; Vesperini 2010). That is, the birth process of a GC can be very violent, depending on the exact initial conditions of its parent gas cloud (Baumgardt & Kroupa 2007; Parmentier & Gilmore 2007; Baumgardt et al. 2008). Therefore, the first few million years can have a significant impact on a GC's evolution over a Hubble time. Marks et al. (2008) find that, depending on the concentration of the initial cluster, gas expulsion can induce a flattening of the stellar mass function of the cluster. Unfortunately, this process cannot be easily computed in a direct way for a GC of the pre-gas expulsive mass of Pal 14, because clusters can lose a large fraction of their birth stellar population as a result of gas expulsion and stellar evolution mass loss. We therefore have to use an approximation here.

Thus, following Marks et al. (2008) and assuming that a certain flattening of the mass function slope has happened within the first

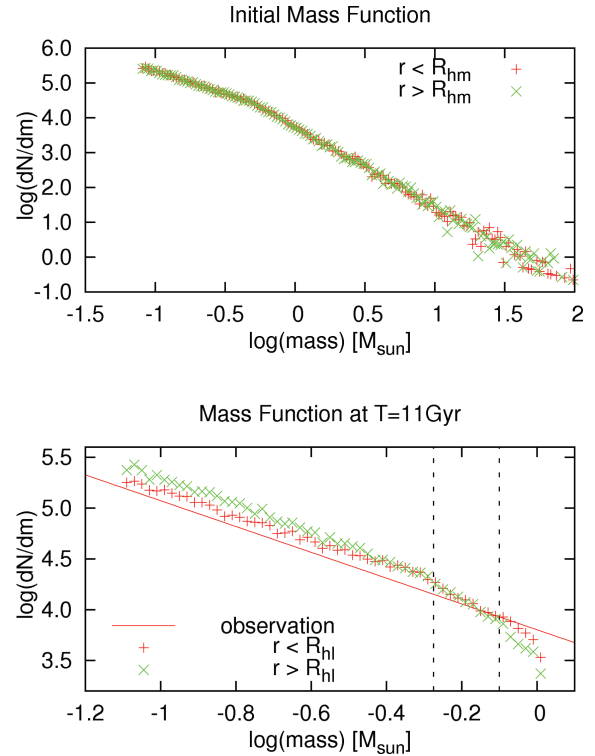


**Figure 5.** Mass function of MS stars for one of the modelled clusters, ‘M50R20’, inside (red pluses) and outside (green crosses) the half-light radius,  $R_{hl}$ . The top panel shows the unsegregated mass function at the start of the simulation which was chosen to be the canonical Kroupa IMF. The observed mass function slope inside the half-light radius is indicated by the solid line. The dotted vertical lines indicate the observed range of stellar mass. The bottom panel shows the mass function after an evolution of 11 Gyr. The slope of the mass function in the observed range is  $1.97 \pm 0.15$ , which is larger than the observed value. The flattened slope of the low-mass part and the steeper slope of the high-mass part within the half-light radius indicate that mass segregation has happened in the cluster.

100 Myr of the cluster's evolution, we change the IMF slope and start the simulations at a cluster age of 100 Myr. In this fashion we have performed a new series of  $N$ -body simulations for models with various flattened initial slopes of the mass function instead of the canonical Kroupa IMF (see overview in Table 2). We have chosen three sets of slopes for the mass function:  $\alpha_a = \{1.7, 0.7\}$ ,  $\alpha_b = \{1.6, 0.6\}$  and  $\alpha_c = \{1.5, 0.5\}$ , where the first number in each set is the slope of the mass function for stars more massive than  $0.5 M_\odot$  and the second one is for low-mass stars (for comparison, the Kroupa IMF is  $\alpha = \{2.3, 1.3\}$ ). The second column in Table 2 shows the name of the simulated models. For example, F0.6M50R20 represents a flattened model with the slope of  $\alpha_b$ , initial mass of  $50\,000 M_\odot$  and initial half-mass radius of 20 pc.

The maximum mass in the mass spectrum was set to  $5 M_\odot$ , instead of  $100 M_\odot$ . The reason can be attributed to the short lifetimes of the most massive stars, i.e. the stars with masses larger than  $5 M_\odot$  will have died or turned into compact remnants within the first 100 Myr. As stated earlier, it is reasonable to assume a retention fraction of 0 per cent for compact remnants due to the low escape velocity from Pal 14.

In Fig. 6 we plot the mass function evolution for one of the best-fitting models, F0.5M50R18. We see that mass segregation has taken place, in addition to our artificial flattening of the mass



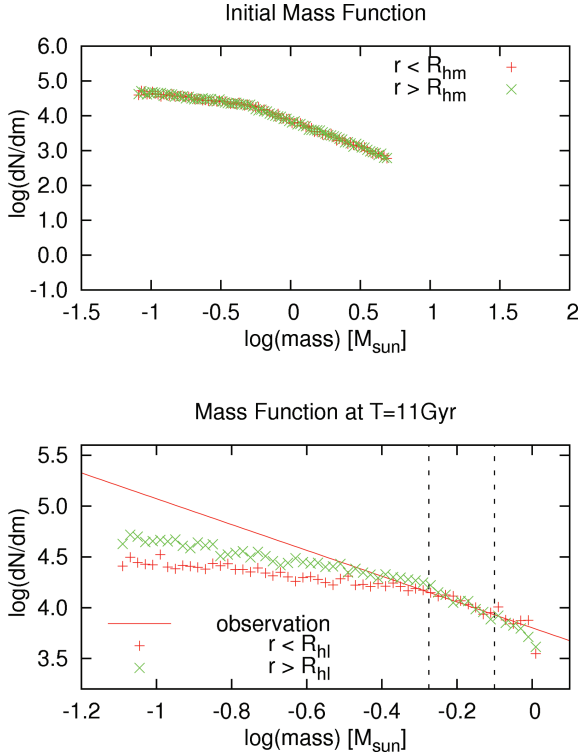


**Figure 6.** The same as Fig. 5, but here we started with a flattened mass function with a slope  $\alpha = 1.5$  above  $0.5 M_{\odot}$ , and  $\alpha = 0.5$  below  $0.5 M_{\odot}$ . The initial mass of this particular model is  $50\,000 M_{\odot}$  and the initial half-light radius is 18 pc. The maximum mass in the mass spectrum was set to  $5 M_{\odot}$ , instead of  $100 M_{\odot}$ . Further properties of the cluster after 11 Gyr of evolution are given in Table 2.

function, by about the same amount as in the non-flattened case in Fig. 5.

The results are summarized in Table 2. We find that a number of models in Table 2 can reproduce the present-day properties of Pal 14. From Fig. 7 we see that all models with a flattened IMF can reproduce the observed slope of the mass function much better. However, the half-light radius, due to the small value of the observational error, can constrain the calculated models. The number of bright stars is also well reproduced in some models. As can be seen in Fig. 7, models with a lower mass and slope pair  $\alpha_a$  as well as models with a higher mass and slope pair  $\alpha_c$  are not compatible with the observed value of  $N_{bs}$ .

In order to calculate the uncertainties of our results, we have simulated each model for several times (i.e. two to six runs for each model). This also gives us some insight to the uncertainties of the models in Section 4.1. The resulting errors are also given in Table 2. These are about the same as the errors of the models in Table 1.

Like in Section 4.1, the line-of-sight velocity dispersion in most of our models is about  $0.6 \text{ km s}^{-1}$  and is compatible with the observed velocity dispersion including or excluding star 15.

As can be seen in Table 2, due to the larger number of massive stars in the clusters with initially flattened mass-function, the average values of  $N_g$  are larger than for clusters with regular initial condition. However, the number of giant stars in some of the best-fitting models (e.g. F0.5M50R20, F0.6M45R18, F0.6M50R18 and F0.7M45R20) are still compatible with the observed value within the uncertainties.

Our best-fitting models of this set (e.g. F0.5M50R18, F0.5M50R20, F0.6M50R18) have lost about  $21\,000 M_{\odot}$  in the five

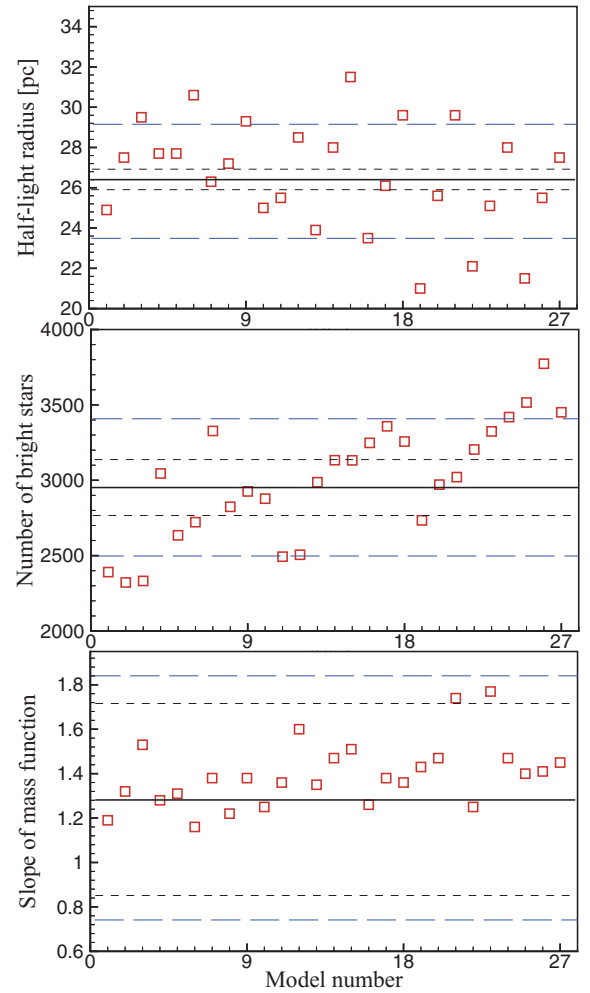


**Figure 7.** The half-light radius (top panel), the number of bright stars (middle panel) and the present-day slope of the mass function for stars with masses between  $0.525$  and  $0.795 M_{\odot}$  (lower panel) for all models with flattened IMFs (Section 4.2). The horizontal axis is the model number listed in Table 2. The horizontal solid and dashed lines indicate the observed values and the corresponding errors, respectively. The horizontal long-dashed lines show the total errors including the typical numerical errors given in Table 2, i.e. points outside these lines are not compatible with the observations. Further properties of the clusters after 11 Gyr of evolution are given in Table 2.

revolutions within the 11 Gyr. This corresponds to a mean mass-loss rate,  $\nu$ , of roughly  $-0.08$ . This means that at each orbit the cluster loses about 8 per cent of its initial mass.

### 4.3 Primordial mass segregation

Another possibility to explain the fact that a standard IMF gives a poor fit to the observed mass function of Pal 14 is the assumption that Pal 14 was primordially mass segregated. To test this hypothesis, we set up clusters with various degrees of mass segregation. The code MCLUSTER allows to specify a degree of mass segregation parameter (hereafter  $S$ ).  $S = 0$  means no segregation and  $S = 1$  refers to full segregation, where the most massive star is in the lowest point of the cluster potential and the least massive star is in the highest point of the cluster potential (Šubr, Kroupa & Baumgardt 2008). MCLUSTER uses the routine described in Baumgardt, De Marchi & Kroupa (2008) to segregate the clusters. This routine allows to

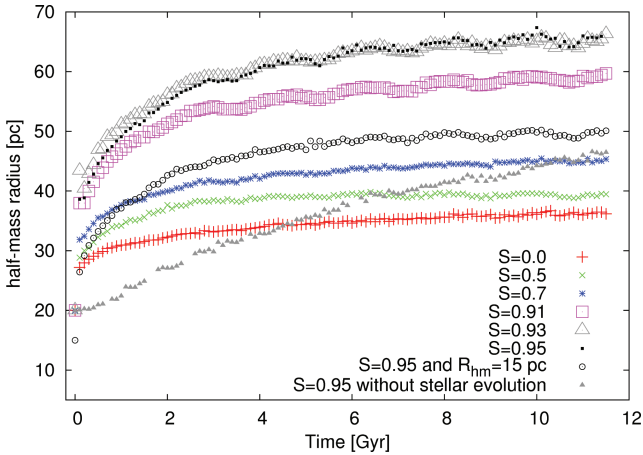


**Figure 8.** Evolution of the 3D half-mass radius for different degrees of primordial mass segregation with a canonical Kroupa IMF. The initial mass is  $50\,000\,M_{\odot}$ , and the initial half-mass radius is 20 pc for all models, except for one model with  $R_{\text{hm}} = 15$  pc. Due to stellar evolution clusters experience a rapid expansion such that clusters with higher degrees of primordial mass segregation experience a larger jump in the half-mass radius within the first 100 Myr of evolution. For comparison, the stellar evolution was artificially switched off for one model. As can be seen, this cluster has no sudden expansion in the beginning of its evolution.

maintain the desired density profile when increasing the degree of mass segregation while also asserting the cluster to be in virial equilibrium.

For this part of the investigation, we take one of our modelled clusters of Section 4.1 and add different degrees of primordial mass segregation. Thus, the initial 3D half-mass radius and initial cluster mass are fixed to  $M = 50\,000\,M_{\odot}$  and  $R_{\text{hm}} = 20$  pc, respectively. The mass segregation parameter was changed in the range  $S = 0.5$ – $0.95$ .

The results of the simulated models are shown in Table 3. In all cases the mass function flattens as the cluster loses stars. The amount of mass function flattening depends on the given amount of mass segregation, i.e. initially more segregated clusters have more flattened mass functions than unsegregated clusters. From Table 3 we see that low values of  $S$  cannot reproduce the observed mass function slope, while highly segregated clusters ( $S \geq 0.9$ ) are able to fit the observed slope of the mass function.

We also find that primordial mass segregation in clusters leads to a stronger expansion than for unsegregated clusters. Fig. 8 shows the evolution of 3D half-mass radius of clusters for different values of the mass segregation parameter. We see that by increasing primordial mass segregation, the final half-mass radius rises. For example, for a mass segregation degree varying between 0.5 to 0.95 and an initial half-mass radius  $R_{\text{hm}} = 20$  pc, the final 3D half-mass radius changes from 39 to 67 pc. This expansion is due to both dynamical and stellar evolution. The stellar evolution in the first 100 Myr has a more important effect and leads to a jump in the cluster’s radius such that the cluster with a higher degree of segregation experiences a larger jump. Consequently, this increase of radius leads to a lower value of the mean velocity dispersion.

In order to reproduce the final  $R_{\text{phl}}$  compatible with the observed value, we therefore have to choose a value for the initial 3D half-mass radius as small as  $R_{\text{hm}} = 15$  pc for a mass segregation parameter of  $S \geq 0.9$ . In this case, the final line-of-sight velocity dispersion in this model is about  $0.6\,\text{km s}^{-1}$ , which is compatible with the observed value. Fig. 9 shows the evolution of the mass

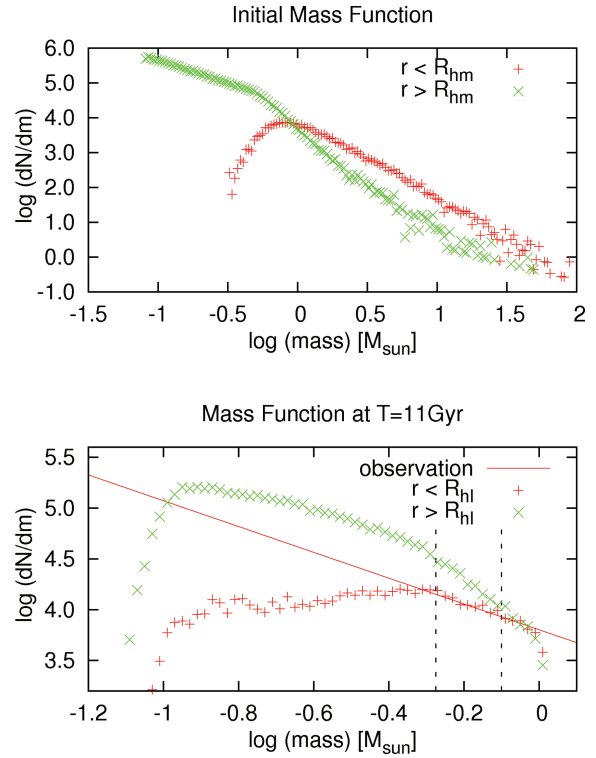


**Figure 9.** The same as Fig. 5, but here we started with a primordially mass segregated cluster with a canonical Kroupa IMF. The initial mass of this particular model (S0.95M50R15) is  $50\,000\,M_{\odot}$ , the initial half-light radius is 15 pc and the mass segregation parameter is set to  $S = 0.95$ . Clusters with such a strong degree of primordial mass segregation are able to reproduce the observed flat mass function inside the half-light radius (solid line).

function of this particular model. The mass function slope after 11 Gyr of evolution reproduces the observations reasonably well. This model can also reproduce all other observational parameters well, but such a high value for the mass segregation parameter implies a very tight correlation of a star’s mass and its specific energy within the cluster at birth. There is no conclusive evidence for such a high degree of primordial mass segregation in any observed star cluster. In addition, as can be seen in Fig. 9, the difference between the slope of the mass function inside and outside the half-light radius is larger than for other models. Thus, further analysis to determine the observed mass function outside the half-light radius would help to distinguish the mass segregation scenario from other scenarios.

The best-fitting model of this set, S0.95M50R15, has lost about  $25\,000\,M_{\odot}$  in the five orbits within the 11 Gyr. This corresponds to a mean mass-loss rate of  $\nu = -0.1$ .

Fig. 10 compares the projected half-light radii,  $R_{\text{phl}}$ , and the projected half-mass radii,  $R_{\text{phm}}$ , for the three different sets of modelled clusters from Sections 4.1 to 4.3. As can be seen, in almost all models  $R_{\text{phl}}$  is smaller than  $R_{\text{phm}}$ . For initially segregated clusters, this difference is more than 10 per cent such that the assumption that mass traces light within a cluster is disputable. It must be mentioned that 10 per cent difference in cluster radius leads to 30 per cent difference in the number of stars, which is significant and should be taken into account in discussions.

#### 4.4 Primordial binaries

Observations and theoretical work suggest that stars may be born with initially very large binary fractions and thus star clusters may

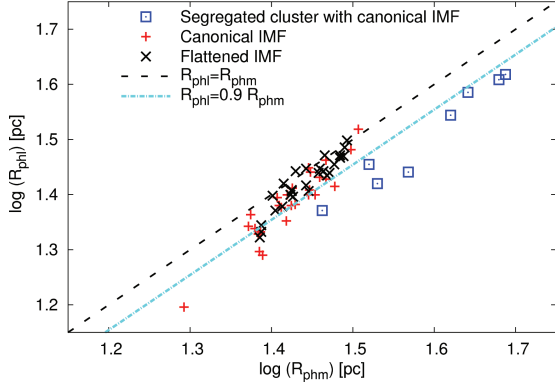


**Figure 10.** The projected half-light radius ( $R_{\text{phl}}$ ) plotted against the projected half-mass radius ( $R_{\text{phm}}$ ) for the different sets of models listed in Tables 1–3. The black dotted line shows the region where  $R_{\text{phl}} = R_{\text{phm}}$ , whereas the cyan dot–dashed line demonstrates if  $R_{\text{phl}}$  is 10 per cent smaller than  $R_{\text{phm}}$ . Initially segregated clusters show more than 10 per cent difference between  $R_{\text{phl}}$  and  $R_{\text{phm}}$ .

contain a significant population of primordial binaries (Kroupa 1995a,b). Low-density stellar systems (i.e. less than  $10^2 \text{ M}_{\odot} \text{ pc}^{-3}$ ) have a binary fraction of at least 50 per cent, while in dense clusters (i.e. more than  $10^4\text{--}10^5 \text{ M}_{\odot} \text{ pc}^{-3}$ ), the binary fraction is less than 10–20 per cent (Hut et al. 1992).

The stellar density in Pal 14 is extremely low ( $0.1\text{--}0.2 \text{ M}_{\odot} \text{ pc}^{-3}$ ), and thus it is expected that most of the primordial binaries survive during the evolution of the cluster. Thus, the present-day binary population could be close to the primordial binary population which it had at birth (Kroupa 1995a,b; Küpper & Kroupa 2010) making Pal 14 a good target to determine the primordial binary fraction of a GC. Here we discuss one model with primordial binaries.

Since tight binaries can significantly speed up the relaxation process, one might be able to explain the flattening of the observed mass function, since by adding binaries, one increases the mean mass of particles in the cluster (as a binary acts like one heavy particle), and by increasing the mean mass we decrease the relaxation time (Heggie & Hut 2003).

Unfortunately, binaries slow down direct  $N$ -body computations immensely because time-steps have to be very small for their integration, such that most numerical investigations neglect binaries completely. It is only the peculiar configuration of Pal 14 with its relatively low mass and low density that enables us to perform such a simulation with a few thousand binaries over a time-span of 11 Gyr. Yet, such a computations takes about one month GPU time on a GeForce GTX 280 GPU.

We set up one of the modelled clusters of Section 4.1 with an initial mass of  $M = 50\,000 \text{ M}_{\odot}$ , initial half-mass radius of  $R_{\text{hm}} = 20 \text{ pc}$ , a canonical Kroupa IMF without primordial mass segregation but with a non-zero primordial binary fraction. We add a few binaries to see if the present-day binary distribution is a good match for the primordial one. A primordial binary fraction,

$$f_{\text{bin}} = \frac{N_{\text{bin}}}{(N_{\text{bin}} + N_{\text{s}})}, \quad (5)$$

of 0.05 (i.e. about 10 per cent of stars being in binaries because  $N_{\text{s}} \gg N_{\text{bin}}$ ), where  $N_{\text{bin}}$  is the number of binary systems in the cluster and  $N_{\text{s}}$  is the number of single stars, is adopted, in order to see how many of them will be destroyed over the course of time and which effect on the cluster’s evolution they have. The initial period distribution (i.e. the post-gas-expulsion period distribution) used in

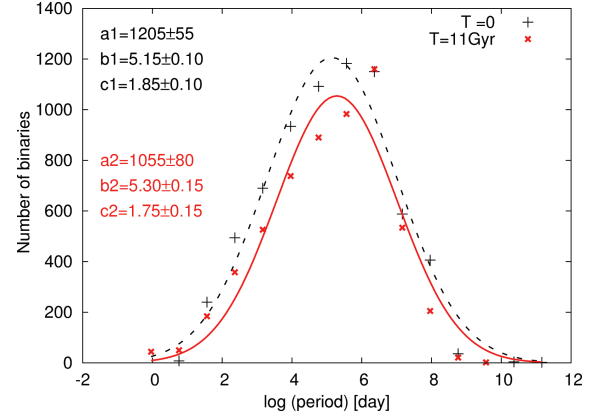


**Figure 11.** The period distribution of bound binary systems found in the cluster at the beginning and after 11 Gyr evolution. Dashed and solid lines are the best Gaussian fits to the initial and final period distributions, respectively. The coefficients of the Gaussian fits with a functional form of  $a \exp[(x - b)^2/2c^2]$  are given in the figure. The errors give the  $1\sigma$  errors. The period distribution stays the same within the errors, showing that dynamical encounters are unimportant in changing the binary population in Pal 14. Almost 85 per cent of primordial binaries have survived the cluster evolution.

this study is the birth period distribution of Kroupa (1995b, 2008). Note that the birth period distribution is not a Gauss function. But the period distribution function of bound binaries (i.e. the widest binary systems are excluded) that results from this birth distribution is approximately a Gauss distribution already at  $T = 0$  Gyr because the widest initial binaries are split due to crowding even in the extremely low density of our initial Pal 14 model.

Our simulation shows that such a small binary fraction does not increase the mass segregation enough, as 5 per cent binaries do not increase the mean mass significantly. Hence, the obtained slope of the mass function, which is about  $\alpha \simeq 2.0$ , is still not compatible with the observed value,  $\alpha = 1.27 \pm 0.44$  within a  $1\sigma$  level of confidence.

After 11-Gyr evolution of the cluster, the binary fraction reaches  $f_{\text{bin}} \simeq 0.04$ , which means that during the evolution most of the binaries ( $\simeq 85$  per cent) survived. In other word, the present-day binary fraction that we see in Pal 14 is almost equal to the primordial binary fraction at its birth. Fig. 11 shows the period distribution of binary systems at the beginning and after 11 Gyr of evolution. The parameters of the best-fitting Gaussian distributions to the initial and final period distributions are presented in Fig. 11. Since the mean period does not change with time (within the error), most of the missing binaries might have escaped the cluster rather than gotten disrupted.

Moreover, adding the binaries increases the mean velocity dispersion such that it reaches  $0.87 \text{ km s}^{-1}$  if we consider all giant stars and MS stars with mass higher than  $0.8 \text{ M}_{\odot}$ . We measure  $0.64 \text{ km s}^{-1}$ , if we add a cut-off in velocities leaving out the stars that are  $5 \text{ km s}^{-1}$  away from the mean and hence would not be considered as cluster members in a cluster like Pal 14. It should be noted that the  $5 \text{ km s}^{-1}$  limit is only applied for this test to compare the velocity dispersion of our model clusters with the observations, since observers would not count stars with such discrepant velocities as members. In all other cases, stars were considered as members only based on their distance to the cluster centre. An overview of the results for this cluster can be found in Table 3. In order to see how well these velocity dispersions are compatible with the observed sample including star 15, we use a KS test again. Here, the  $P$ -value is 0.68

for both cases with and without adding the cut-off for high-velocity stars. This means that the data presented in Jordi et al. (2009) is compatible with our modelled cluster with primordial binaries with 68 per cent confidence. This is compatible with recent results by Küpper & Kroupa (2010).

## 5 CONCLUSIONS

We performed a series of  $N$ -body computations in order to create a realistic model for the outer halo GC Pal 14 and show that it is possible nowadays to directly calculate the evolution of small Milky Way GCs over a Hubble time by direct  $N$ -body simulations. For the sake of comparison, and as a rough estimate, the modelling of a typical halo GC (i.e. with the initial mass of about  $2 \times 10^5 M_\odot$  and half-light radius of about 5 pc) over 12 Gyr will take about  $10^5$  times longer than Pal 14, given the same resources. Moreover, about half of the Galactic halo GCs are located at  $R_G < 6$  kpc, hence the tidal field and cluster evaporation would be stronger, thereby implying a higher initial cluster mass and longer time of simulation.

Pal 14's large radius together with its low mass, thus low density, allows us to simulate it on a star-by-star basis. In this way we are not only able to learn more about the dynamical history of such kind of GCs, but are also able to study the process of cluster formation as this period leaves its imprint on its ensuing evolution. Moreover, we show that there is valuable synergy between simulations and observations, as simulations can make predictions for observations and, on the other hand, can test observational parameters on their consistency.

Therefore, we generated 66 models divided into four categories: clusters with a canonical Kroupa IMF (Section 4.1), clusters with a flattened IMF (Section 4.2), clusters with a Kroupa IMF but with primordial mass segregation (Section 4.3) and finally one cluster with primordial binaries (Section 4.4). By varying the initial half-mass radius and the initial mass of the model clusters, we searched through parameter space to obtain the model that matches the available observations of Pal 14 best.

We used the most recent observational data to constrain the modelled clusters. Thus, for all simulated clusters we compared the half-light radius, the total number of bright stars inside the half-light radius and the present-day mass function slope inside the half-light radius in the mass range  $0.5\text{--}0.8 M_\odot$  with the observed values. Furthermore, we checked the line-of-sight velocity dispersion and the number of giant stars for their consistency with the numerical results.

From the computations, we find that all clusters segregate significantly over the course of time, although the relaxation time of Pal 14 is longer than a Hubble time. We furthermore find that this mass segregation leads to an increasing flattening of the mass function inside half-light radius, which is what we were looking for since the observational value for the mass function slope of Pal 14 in the respective regime is only  $\alpha = 1.27 \pm 0.44$  (Jordi et al. 2009) compared to a Kroupa IMF value of 2.3. The initially unsegregated clusters with a canonical Kroupa IMF do not produce enough depletion in the slope of the mass function in order to be in good agreement with the observations, though. Only a few models of this set marginally agree within the uncertainties with this value for  $\alpha$ . Besides that, the other observational constraints are matched reasonably well by most of the models in this set (Table 1 and Fig. 3).

The models with the flattened IMFs can make up for the discrepancy in  $\alpha$ , though some of them fail in the other parameters (Table 2 and Fig. 7). Primordial mass segregation also increases the flatten-

ing of the mass function but the necessary degree of primordial mass segregation turns out to be very high (Table 4.3).

The initially flattened mass function can be explained by the loss of low-mass stars from an initially mass-segregated cluster across the tidal radius during the gas-expulsion phase (Marks & Kroupa 2010). Therefore, the flattened IMF of Pal 14 we uncover here strengthens the idea that this cluster formed in a stronger tidal field rather than in isolation. This may have been the case if either the Galactic tidal field has since then evolved, or if the cluster was born closer to the Galactic Centre (eccentric orbit), or, more speculatively, the cluster birth site was a now detached/disrupted dwarf galaxy. However, if Pal 14 has always been on the same circular orbit, it is hard to imagine that the tidal field would have played a role during the cluster response to gas expulsion (Parmentier & Kroupa 2010). Primordial binaries ( $f_{\text{bin}} = 0.05$ ) do not help to reproduce the observational value of the mass function.

Thus, we are able to find some scenarios that can reproduce all observations reasonably well. We find that the initial mass of Pal 14 was about  $50\,000 M_\odot$  and that it started with a half-mass radius of about 20 pc. The cluster must have been significantly mass-segregated with stellar mass function depleted in low-mass stars. These are the signatures of a post-gas expulsion cluster (Marks et al. 2008). The inferred post-gas expulsion 'initial' half-mass radius is larger than the half-mass radii of most GCs which is of the order of 3 pc. Moreover, we show that the different scenarios show different mass functions outside the half-light radius, such that finding the observational value for this region would help to discriminate between the different scenarios.

The effect of unresolved binaries is an important issue that has to be considered in the observational values of the velocity dispersion and the mass function. If Pal 14 has a significant binary population, which we expect due to the low density of this cluster, the true (binary-corrected) mass function should be steeper, because of the existence of unresolved components (Kroupa, Gilmore & Tout 1991). Therefore, the slope of the mass function is the most uncertain parameter of the observations of Pal 14. Even without taking binaries into account, Jordi et al. (2009) estimate the uncertainty to be  $\simeq \pm 0.4$ . Furthermore, as Küpper & Kroupa (2010) have shown, if the binary fraction was normal (i.e. more than 50 per cent), the binary-corrected velocity dispersion of the cluster would also be smaller than the value reported by Jordi et al. (2009).

From the set of computations we furthermore find that primordial mass segregation leads to a larger impact of stellar evolution on cluster expansion. This is, segregated clusters are more affected by mass loss through stellar evolution (Fig. 8). We furthermore quantify the effect of mass segregation on the ratio of half-mass radius to half-light radius and find the latter to be up to 10 per cent smaller (Fig. 10), leading to significant observational uncertainties for the number of stars within this radius in such cases.

Moreover, we measured the line-of-sight velocity dispersions of our models taking into account all stars, and compared it with the observed values. We additionally measured the velocity dispersion considering only giant stars, and find that both values do not show significant difference between each other, showing that giant stars are good tracers of a cluster's global velocity dispersion. Most clusters show a velocity dispersion of  $\simeq 0.6 \text{ km s}^{-1}$ , suggesting that star15 of the sample of Jordi et al. (2009) might be a normal cluster member.

Finally we find from the model with a primordial binary fraction of 5 per cent that due to the low stellar density of Pal 14 the initial binary distribution stays almost unchanged by the dynamical

evolution of the cluster, and only about 15 per cent of binaries escape or get disrupted in the course of time (Fig. 11). Low-density clusters like Pal 14 are therefore good objects to study the primordial binary distribution of GCs.

## ACKNOWLEDGMENTS

AHZ and HH thank the Stellar Population and Dynamics Group of the Argelander Institute for Astronomy and the Institute for Advanced Studies in Basic Sciences (IASBS) for providing financial support for this research. HB acknowledges support from the German Science Foundation through a Heisenberg Fellowship and from the Australian Research Council through Future Fellowship grant FT0991052.

## REFERENCES

- Aarseth S. J., 2003, *Gravitational N-Body Simulations*. Cambridge Univ. Press, Cambridge
- Anders P., Lamers H. J. G. L. M., Baumgardt H., 2009, *A&A*, 502, 817
- Baumgardt H., Kroupa P., 2007, *MNRAS*, 380, 1589
- Baumgardt H., Makino J., 2003, *MNRAS*, 340, 227
- Baumgardt H., Grebel E. K., Kroupa P., 2005, *MNRAS*, 359, L1
- Baumgardt H., De Marchi G., Kroupa P., 2008a, *ApJ*, 685, 247
- Baumgardt H., Kroupa P., Parmentier G., 2008b, *MNRAS*, 384, 1231
- Bonnell I. A., Davies M. B., 1998, *MNRAS*, 295, 691
- De Marchi G., Paresce F., Pulone L., 2007, *ApJ*, 656, L65
- Dekker H., D'Odorico S., Kaufer A., Delabre B., Kotzłowski H., 2000, *Proc. SPIE*, 4008, 534
- Dotter A., Chaboyer B., Jevremovic D., Baron E., Ferguson J. W., Sarajedini A., Anderson J., 2007, *AJ*, 134, 376
- Dotter A., Sarajedini A., Yang S.-C., 2008, *AJ*, 136, 1407
- Elmegreen B. G., 2004, *MNRAS*, 354, 367
- Gentile G., Famaey B., Angus G., Kroupa P., 2010, *A&A*, 509, A97
- Giersz M., Heggie D. C., 2009, *MNRAS*, 395, 1173
- Goodwin S. P., 1997, *MNRAS*, 286, 669
- Goodwin S. P., 1998, *MNRAS*, 294, 47
- Haghi H., Baumgardt H., Kroupa P., Grebel E. K., Hilker M., Jordi K., 2009, *MNRAS*, 395, 1549
- Harfst S., Portegies Zwart S., Stolte A., 2010, *MNRAS*, 409, 628
- Harris W. E., 1996, *AJ*, 112, 1487
- Heggie D. C., Hut P., 2003, *The Gravitational Million-Body Problem*. Cambridge Univ. Press, Cambridge
- Hilker M., 2006, *A&A*, 448, 171
- Hurley J. R., Pols O. R., Tout C. A., 2000, *MNRAS* 315, 543
- Hut P. et al., 1992, *PASP*, 104, 981
- Jordi K. et al., 2009, *AJ*, 137, 4586
- King I. R., 1966, *AJ*, 71, 64
- Kroupa P., 1995a, *MNRAS*, 277, 1491
- Kroupa P., 1995b, *MNRAS*, 277, 1507
- Kroupa P., 2001, *MNRAS*, 322, 231
- Kroupa P., 2002, *Sci*, 295, 82
- Kroupa P., 2008, *The Cambridge N-Body Lectures*. *Lecture Notes in Phys.*, 760, 181
- Kroupa P., Boily C. M., 2002, *MNRAS*, 336, 1188
- Kroupa P., Gilmore G., Tout C. A., 1991, *MNRAS*, 251, 293
- Kruijssen J. M. D., Mieske S., 2009, *A&A*, 500, 785
- Krumholz M. R., Klein R. I., McKee C. F., Offner S. S. R., Cunningham A. J., 2009, *Sci*, 323, 754
- Küpper A. H. W., Kroupa P., 2010, *ApJ*, 716, 776
- Marks M., Kroupa P., 2010, *MNRAS*, 406, 2000
- Marks M., Kroupa P., Baumgardt H., 2008, *MNRAS*, 386, 2047
- Mouri H., Taniguchi Y., 2002, *ApJ*, 580, 844
- Parmentier G., Gilmore G., 2007, *MNRAS*, 377, 352
- Parmentier G., Kroupa P., 2010, *MNRAS*, in press
- Parmentier G., Goodwin S. P., Kroupa P., Baumgardt H., 2008, *ApJ*, 678, 347
- Salpeter E. E., 1955, *ApJ*, 121, 161
- Sarajedini A., 1997, *AJ*, 113, 682
- Šubr L., Kroupa P., Baumgardt H., 2008, *MNRAS*, 385, 1673
- Tan J. C., Krumholz M. R., McKee C. F., 2006, *ApJ*, 641, L121
- Trenti M., Vesperini E., Pasquato M., 2010, *ApJ*, 708, 1598
- Vesperini E., 2010, *Philos. Trans. R. Soc. A: Math. Phys. Eng. Sci.*, 368, 829
- Vesperini E., Heggie D. C., 1997, *MNRAS*, 289, 898
- Vesperini E., McMillan S., Portegies Zwart S., 2009, *ApJ*, 698, 615
- Vogt S. S. et al., 1994, *Proc. SPIE*, 2198, 362

This paper has been typeset from a  $\text{\LaTeX}$  file prepared by the author.

Copyright of Monthly Notices of the Royal Astronomical Society is the property of Wiley-Blackwell and its content may not be copied or emailed to multiple sites or posted to a listserv without the copyright holder's express written permission. However, users may print, download, or email articles for individual use.